Bioactive Materials 49 (2025) 193–206

Contents lists available at ScienceDirect

Bioactive Materials

journal homepage: www.keaipublishing.com/en/journals/bioactive-materials

A self-accelerating 'copper bomb' strategy activated innate and adaptive immune response against triple-negative breast cancer

Xinzhi Xu [a,b,1], Hang Zhou [a,1], Ruixia Hong [a], Jiaqi Gong [a], Yujie Wan [a], Qihuan Fu [a], Kaifeng Huang [a], Ying Li [a], Na Wang [a,c], Peng Zhao [b,**], Kaiyong Cai [b,***], Fang Li [a,*]

[a] Department of Ultrasound, Chongqing University Cancer Hospital, Chongqing 400030, China
[b] Key Laboratory of Biorheological Science and Technology, Ministry of Education, College of Bioengineering, Chongqing University, Chongqing 400044, China
[c] School of Medicine, Chongqing University, Chongqing, China

ARTICLE INFO

Keywords:
Cuproptosis
Proteotoxic stress
mtDNA-cGAS-STING pathway
Triple-negative breast cancer
Immune response

ABSTRACT

Triple-negative breast cancer (TNBC) presents therapeutic challenges due to its aggressive, drug-resistance, and low immunological reactivity. Cuproptosis, an emerging therapeutic modality, is a promising strategic intervention for treating TNBC. Nonetheless, the effectiveness of cuproptosis is compromised by tumor adaptations, including the Warburg effect, increased intracellular glutathione (GSH), and copper efflux, thus breaking the barrier of cuproptosis is the basis for developing cuproptosis-based clinical therapies. Herein, a self-accelerating strategy utilizing a pH-responsive copper framework encapsulating glucose oxidase (GOx), modified with polyethylene glycol (PEG) and tumor-penetrating peptide (tLyp1) has been developed. Upon reaching the acidic tumor microenvironment, the released GOx increases intracellular acidity and hydrogen peroxide (H_2O_2). The elevated intracellular GSH and H_2O_2 serve as "fuel" to amplify the copper-based catalytic within tumor cells. Concurrently, the reduction of copper efflux proteins (ATP7B) and the depletion of GSH lead to copper overload in tumor cells, leading to cuproptosis via copper overload, mitochondrial disruption, and Fe-S protein instability. This constellation of interrelated events constitutes a potent "Copper Bomb," which concurrently triggers the immune system and effectively kills the tumor. It robustly engages innate and adaptive immunity via the release of mitochondrial DNA, facilitating the cGAS-STING pathway and precipitating immunogenic cell death. This process reverses the immunosuppressive tumor microenvironment, eliminates tumor cells, and suppresses metastasis, thus offering a novel therapeutic modality for the comprehensive treatment of triple-negative breast cancer (TNBC).

1. Introduction

Breast cancer is the most prevalent malignant tumor worldwide [1], with triple-negative breast cancer (TNBC) representing the most lethal and aggressive subtype [2]. TNBC evolved to acquire specific antioxidant defense functions [3], high glycolysis [4], and susceptibility to drug resistance [5], which collectively constrain therapeutic options. Chemotherapy is the main treatment for TNBC, but it is prone to drug resistance and severe side effects [6]. Despite the success of immunotherapy in improving survival across various solid tumors, the response rate to single-agent immune checkpoint inhibitors in TNBC is negligible, at only 5 % [7], attributable to the heterogeneity. Thus, there is an urgent requirement for novel therapeutic approaches to optimize the clinical care of TNBC patients.

Cuproptosis, a regulated cell death mediated by copper, is a promising therapeutic strategy for tumor treatment [8]. Copper directly binding to the lipoylated dihydrolipoamide S-acetyltransferase (DLAT) of the tricarboxylic acid (TCA) cycle causes aggregation and Fe-S cluster protein degradation, ultimately leading to cell death [9], overcoming apoptotic resistance and the limitations of conventional chemotherapies

Peer review under the responsibility of KeAi Communications Co., Ltd.
* Corresponding author.
** Corresponding author.
*** Corresponding author.
E-mail addresses: peng.zhao@cqu.edu.cn (P. Zhao), kaiyong_cai@cqu.edu.cn (K. Cai), lifang0703@cqu.edu.cn (F. Li).
[1] means these authors contributed equally to this article, which means that Xinzhi Xu and Hang Zhou as co-first author.

https://doi.org/10.1016/j.bioactmat.2025.02.019
Received 29 October 2024; Received in revised form 8 February 2025; Accepted 11 February 2025

[10]. Cuproptosis induces immunogenic cell death (ICD), modulating the tumor microenvironment (TME) by exposing DAMPs and promoting T-lymphocyte infiltration [11]. Concurrently, cuproptosis also disrupts mitochondrial respiration [12], leading to proteotoxic stress, mitochondrial membrane damage, and mitochondrial DNA (mtDNA) release into the cytosol [13]. Cytosolic DNA is detected by cyclic GMP-AMP synthase (cGAS), and subsequent activation of the stimulator of interferon genes (STING) pathway [14], suggesting that mtDNA released due to mitochondrial proteotoxic stress is likely to activate the cGAS-STING signaling pathway [15–17]. This activation induces the secretion of pro-inflammatory type I interferons (IFNs) and promotes the maturation and activation of antigen-presenting cells (APCs) and natural killer cells (NKs) [18,19]. This process may elicit a robust anti-tumor immune response via the mtDNA-cGAS-STING axis and ICD, warranting further systematic investigation. However, the therapeutic effect of cuproptosis faces challenges, including inhibition by GSH [20], reduced sensitivity due to the Warburg effect [21], and limited clinical utility of copper carriers [22]. Therefore, developing strategies to deplete GSH and enhance mitochondrial respiration to activate cuproptosis is a critical priority.

Glucose oxidase (GOx)-mediated starvation therapy depletes glucose and ascends TME acidity, hypoxia, and H_2O_2 levels [23]. This treatment sensitizes TNBC cells to cuproptosis by disrupting glycolysis and stimulating mitochondrial respiration, while in situ production of H_2O_2 increasing oxidative stress [24], generated H_2O_2 can be further converted via copper into hydroxyl radicals (·OH), leading to tumor cell death [25]. GOx also reduces ATP, lowering ATP7B expression, a key of copper exporter protein [26]. A nanoplatform combining GOx with cuproptosis agents is expected to induce a self-accelerating therapeutic effect, effectively eliminating tumor cells.

In this study, we propose a "self-accelerating" strategy for initiating a starvation therapy-cuproptosis cycle for anti-tumor therapy and activation immunity. Firstly, we synthesized copper-doped mesoporous silica nanoparticles (MCNs) via a hydrothermal process, resulting in a pH-responsive sea urchin-like structure. GOx was adsorbed onto the MCNs' surface. For enhanced stability, tumor targeting, and penetration, the GOx@MCNs were functionalized with silane-PEG-tLyp1 to form nanosystem, which we named CGNPs (Scheme 1a). CGNPs accumulate in tumors via the EPR effect and tLyp1-mediated penetration. Once internalized, the CGNPs acted as a highly selective "copper bomb" ignited by the tumor-specific low pH environment, releasing GOx and Cu^{2+}, resulting in cellular acidification, elevated H_2O_2 levels, and reduced ATP. The increased acidity triggers the degradation of the CGNPs framework, fully releasing the loaded Cu^{2+}, which initiates a Fenton-like reaction with H_2O_2 to produce toxic ·OH and Cu^{+}. This process is amplified by the interaction between Cu^{2+} and GSH, establishing a cyclic cuproptosis-inducing mechanism. GOx modulates tumor cell metabolism, enhancing mitochondrial respiration and creating a

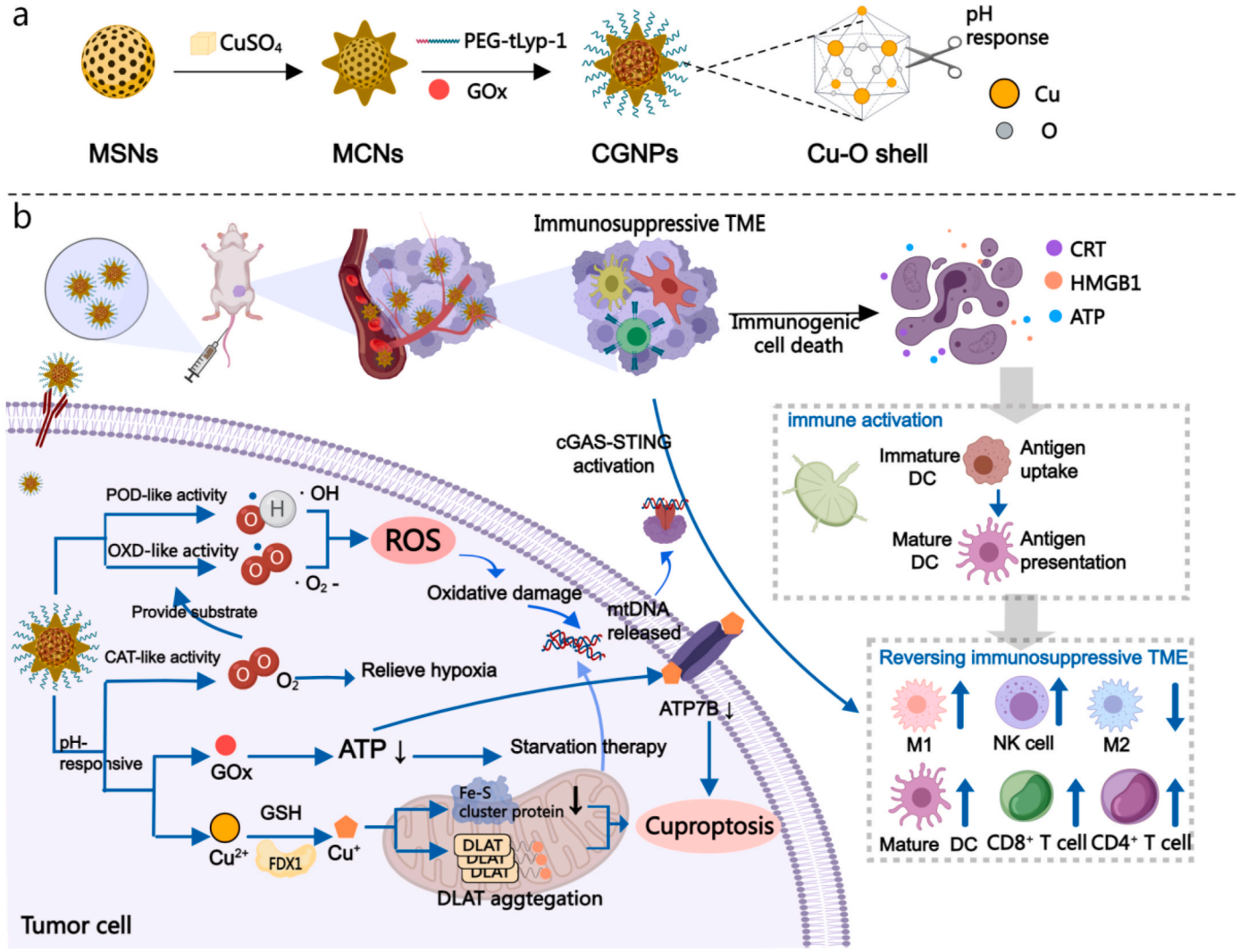

Scheme 1. Schematic illustration of the process of preparation of CGNPs nanoplatforms(a), and the strategy of "copper-bomb" for potent antitumor therapy and activated immunity response through a self-accelerating cycle of starvation therapy-cuproptosis (b).

self-accelerating cycle of starvation therapy-cuproptosis with potent anti-tumor effects. The disruption of the mitochondrial respiratory chain by Cu^{+} induces proteotoxic stress, facilitating mtDNA release to cytosolic and activation of the cGAS-STING pathway, which activates innate and adaptive immunity response, promotes DC maturation, NK activation, T cell priming, remodeling the immunosuppressive TME and inhibiting tumor progression and metastasis through a comprehensive immune activation strategy (Scheme 1b).

2. Experimental methods

2.1. Fabrication of mesoporous copper-doped nanoparticles (MCNs)

Using hydrothermal process synthesize MCNs. Initially, CTAC (2 g) and TEA (0.02 g) were dissolved in deionized water (20 mL) at 80 °C stirring for 20 min. TEOS (1.5 mL) was then dropped into the solution, and the reaction was allowed to continue for another 4 h at 80 °C with stirring (350 rpm), the white products were collected by centrifugation (18,000 rpm) and were extracted three times with hydrochloric acid and ethanol (1:9) at 60 °C. Next, the products (65 mg) and Cu $[NO_3]_2{\cdot}3H_2O$ (169 mg) were premixed in deionized water (40 mL) with 20 min, followed by the dropwise addition of $NH_3{\cdot}H_2O$ (30 wt %, 6 mL). The mixed solution was held in a heating oven at 140 °C for 10 h. Finally, the blue products were precipitated by centrifugation (18,000 rpm, 15 min) and vacuum drying at 60 °C.

2.2. Fabrication of GOx-loaded MCNs (CGNPs)

MCNs (2 mg) were dispersed in a GOx solution (2 mL, 2 mg/mL) with stirring at room temperature for 24 h. The product was collected by centrifugation (18,000 rpm, 15 min) and washed three times with ethanol and PBS, which we named MCNs@GOx nanoparticles (CGNPs).

2.3. Surface modification of CGNPs

Anchoring mal-PEG-silane to the surface of the CGNPs for increase the stability. Typically, CGNPs (10 mg) were dispersed in an ethanol solution (100 mL, mal-PEG-silane, 0.5 mg/mL) stirring at 50 °C for 24 h. PEGylated CGNPs were collected by centrifugation (18,000 rpm, 15 min). Using thiol-maleimide reaction is formed through the cys bond of tLyp-1 and the mal bond of the PEG. 10 mg CGNPs-PEG-mal mix with 0.5 μmol tLyp-1 at a concentration of 5 mg/mL, incubated overnight at 4 °C. Then the unreacted peptides in the solution were removed by centrifugation (18,000 rpm, 15 min). To facilitate observation of CGNPs, adding FITC fluorescent for label. Typically, CGNPs (20 mg) and FITC (100 mg) were dispersed in an ethanol solution (100 mL) stirring for 24 h at room temperature. The FITC-labeled products were collected by centrifugation (18,000 rpm, 10 min) and washed three times.

2.4. Cellular uptake and subcellular localization measurement

As for cellular uptake, the MDA-MB-231 cells were seeded on Confocal Dish and incubated for 24 h, then the culture medium was aspirated, and the fresh culture medium containing the CGNPs (100 μg/mL) was incubated for 0.5 h, 1 h and 2 h, respectively, then washed with PBS solution for 3 times, stained with DAPI, fixed with tissue fixative, and the fluorescence images were recorded with a CLSM.

As for subcellular localization, the MDA-MB-231 cells were seeded on confocal dish and incubated for 24 h, then the fresh culture medium containing the CGNPs (100 μg/mL) was incubated for 4h and 12h, respectively. Then collection cells and use glutaraldehyde fixed cell, and the images were recorded with a Bio-TEM. The MDA-MB-231 cells was incubated with CGNPs(100 μg/mL) for 1h, 2h, 4h and 6h, respectively. Then stained with Lysotraker Blue, and the fluorescence images were recorded with a CLSM.

2.5. Cu^{+} released and subcellular localization measurement

The MDA-MB-231 cells were seeded onto a Confocal Dish and incubated for 24 h. After incubation, the culture medium was aspirated, and the cells were treated with fresh culture medium containing CGNPs at a concentration of 100 μg/mL for 0, 2, 4, and 8 h, respectively. Subsequently, the cells were washed three times with PBS, stained with LysoTracker Blue for 1 h, and then washed again with PBS. Following this, the cells were stained with MitoTracker Orange for 30 min, washed with PBS, and then stained with CuprosGreen for 3 h. Finally, fluorescence images were recorded using a confocal laser scanning microscope (CLSM).

2.6. Effect of CGNPs on DC maturation and macrophage M1 repolarization

First, BMDMs and BMDCs were obtained from the bone marrow of 6-week-old BALB/c female mice. The isolation, formation, and M2-polarized activation of BMDMs were accomplished by the previously reported [27]. The acquisition of immature BMDCs were as the same as the classical Lutz's method. To study the effects of CGNPs on immature DC and M2 polarized macrophages while avoiding the impact of CGNPs on immune cells, we used Transwell chambers. Firstly, M2 polarized macrophages and immature DC cells were seeded at a density of $5*10^5$/cell in the lower chambers of a six-well plate, followed by overnight co-incubation with 4T1 cells in the up-chambers. The culture medium in the up-chambers was replaced with 1640 containing 100 μg/ml of CGNPs. After co-incubation for 12 h, the medium was replaced with fresh culture medium, and the immune cells were collected 24 h later for analysis. Flow cytometry was used to assess M1 repolarization of macrophages and BMDC maturation, with labeling for M1 macrophages ($CD11b^{+}CD86^{high}CD206^{low}$), M2 macrophages ($CD11b^{+}CD86^{low}CD206^{high}$), mature DC cells ($CD11c^{+}$ $CD86^{+}$), and immature DC cells ($CD11c^{+}CD86^{-}$). Meanwhile, the supernatant was collected for ELISA to assess cytokine release. The pro-inflammatory cytokines (TNF-α and IL-12p70 released by mature BMDCs, TNF-α and IFN-β released by M1-polarized BMDMs) in the culture medium were examined by ELISA.

2.7. mtDNA release by confocal microscopy

The cells were seeded in confocal dished at a density of 1×10^5 per well. After culturing for 24 h, the cells were treated with PBS, GOx, MCNs or CGNPs (100 μg/mL) for 24 h. Then the cells were stained by 3 μL/mL PicoGreen (Invitrogen, USA) and 100 nM MitoTracker Red (Invitrogen, USA) for 30 min and fixed by 4 % PFA. The fluorescent images were obtained by CLSM.

2.8. Assess the ability to remold the immunosuppressive tumor microenvironment

As for tumor, using CytoFlexLX flow cytometer after dissociating the tumor tissue into a single-cell suspension, M1 macrophages, M2 macrophages, helper T lymphocytes ($CD3^{+}$ $CD4^{+}$), cytotoxic T lymphocytes ($CD3^{+}$ CD8α+), and NK cells ($CD49b^{+}$ $CD3^{-}$). The lymph node was used to assessment DC mature (mature DC: $CD80^{+}CD86^{+}$). For assessment of long-term immune-memory effects after therapy, the spleens were collected and prepared into a single-cell suspension. Effector memory T cells ($CD3^{+}$ $CD8^{+}$ $CD44^{+}$ $CD62L^{-}$) (Tem) and central memory T cells ($CD3^{+}$ $CD8^{+}$ $CD44^{+}$ $CD62L^{+}$) (Tcm) were examined by FCM after staining. At the same time, TNF-α, IFN-γ, IL-6, IFN-β, and IL-12p70 in primary tumors were examined by ELISA kits.

3. Result and discussion

3.1. Cuproptosis-related gene expression and immune microenvironmental analysis of TNBC

Cuproptosis has been evaluated in various tumor models, including bladder cancer, colorectal cancer, and glioblastoma multiforme [28,29]. Our analysis of The Cancer Genome Atlas and Genotype-Tissue Expression datasets revealed significant differences in the expression of cuproptosis-related genes in triple-negative breast cancer (TNBC) compared to normal tissues (Fig. 1a). Bioinformatics analysis indicated that the expression of FDX1 and DLAT displaying particularly high expression compared to other subtypes of breast cancer. ATP7B, the major efflux protein of copper ions, is an important factor limiting the occurrence of cuproptosis. TNBC has similar expression to normal breast tissues, whereas ERα-positive breast cancers have significantly higher ATP7B expression. Bioinformatics analysis showed that TNBC had relatively high expression of cuproptosis-acting proteins and low expression of efflux proteins. These findings suggest that TNBC may exhibit enhanced sensitivity to cuproptosis. To corroborate this hypothesis, we conducted immunohistochemical analysis on patient sections (Fig. 1b), which revealed a significantly higher expression of DLAT and FDX1 in TNBC compared to both normal tissue and ERα-positive breast cancer, consistent with bioinformatics analysis, ATP7B expression in TNBC did not show a significant elevation compared to normal tissue. Furthermore, the CIBERSORT score heat map analysis of TNBC indicated poor immune infiltration (Fig. 1c), highlighting the immunosuppressive microenvironment characteristic of this subtype. The activation of immunogenic cell death (ICD) and the remodeling of the immunosuppressive microenvironment in combination with cuproptosis represent a promising novel therapeutic approach for TNBC.

3.2. Preparation and Characterization of CGNPs

Precisely engineered pH-responsive copper-doped mesoporous silica nanoreactors (MCNs) were fabricated as illustrated in Fig. 2a. Through a straightforward hydrothermal process, Cu^{2+} was integrated into the MSNs framework, yielding sea urchin-like nanostructures as depicted in Fig. 2b. High-angle annular dark-field scanning TEM images and elemental mapping (Fig. 2c) demonstrated the uniform distribution of Cu within the MCNs framework. X-ray photoelectron spectroscopy (XPS) showed (Fig. 2d and e) the presence of two strong Cu^{2+} satellites at 944.7 and 963.1 eV for Cu 2p spectrum. XRD (Fig. 2f) patterns showed several broadened peaks, which could be assigned to the $CuSiO_3{\cdot}3H_2O$ phase (JCPDS No. 32–0346) and CuO phase (JCPDS No.48-1548), which demonstrates the successful loading of Cu^{2+} into the framework and the formation of CuO, which ensures that the subsequent pH response. The hydrodynamic particle size of the MCNs was measured at approximately 93 nm. Following the encapsulation of GOx and the conjugation with polyethylene glycol (PEG), which we named MCNs@GOx nanoparticles (CGNPs), the hydrodynamic particle size increased to 182 nm (Fig. 2g–Table S1). The high dispersion and nano-diameter ensured that the CGNPs could directly reach the tumor. The doping amount of Cu^{2+} in MCNs was 20.7 % (Fig. S1), determined by ICP-OES, and the loading of GOx was 22.56 % (Fig. S2), measured by a UV spectrophotometer. Fourier transform infrared spectroscopy (FT-IR) confirmed the successful modification of MCNs with PEG, as depicted in Fig. 2h, ensuring prolonged circulation in vivo. Upon localization within the TME, where the pH is slightly acidic, the Cu-O bond within the CGNPs carrier structure is disrupted by H^+, leading to the dissolution of the nanoreactors as depicted in Fig. 2i. To simulate the in vivo TME conditions, CGNPs were exposed to phosphate-buffered saline (PBS) solutions with pH 6.5, and TEM and particle size monitored degradation. The results showed that the nanostructures in pH 6.5 showed significant damage after 24 h, with the disappearance of the sea urchin structure and solidification and deformation of the nanoparticles (Fig. 2j). This was verified by the particle size, which showed significant aggregation of CGNPs due to structural disintegration after 48h in a weakly acidic solution (Table S1). In addition, CGNPs under weakly acidic conditions were able to release GOx (Fig. 2k) and Cu^{2+} (Fig. 2l) from the framework more efficiently and rapidly. This suggests that the strategy enables simultaneous, in situ release of GOx and Cu^{2+}, thereby reducing off-target effects and systemic toxicity.

3.3. Evaluation of self-accelerating and cell phagocytosis of CGNPs in vitro

TNBC is insensitive to oxidative stress damage due to its antioxidant defense mechanism. Therefore, we designed CGNPs to disrupt its antioxidant defense system through self-accelerating starvation therapy-

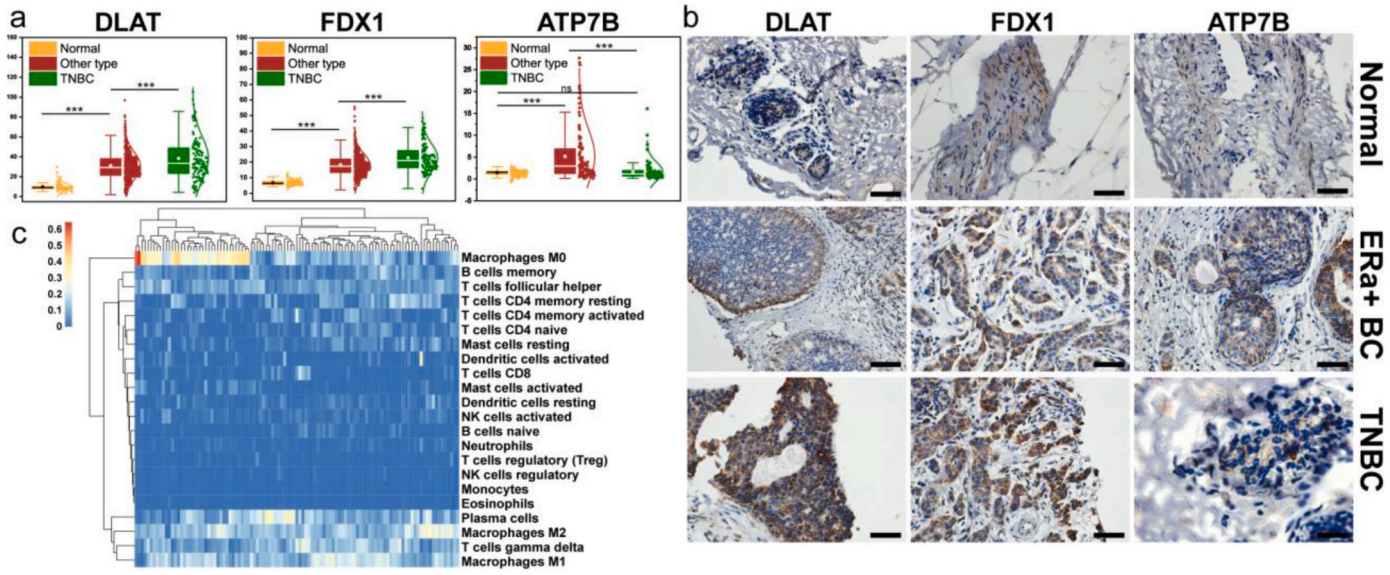

Fig. 1. Bioinformatics analysis of cuproptosis and immune TME in TNBC a). Bioinformatic analyses of cuproptosis-related genes (FDX1, DLAT and ATP7B) in TNBC, other types of breast cancer and normal breast tissue; b). IHC of patient tissue sections of DLAT, FDX1 and ATP7B (Scale bar = 50 μm); c). CIBERSORT score heat map of TNBC. *p < 0.05; **p < 0.01; ***p < 0.001.

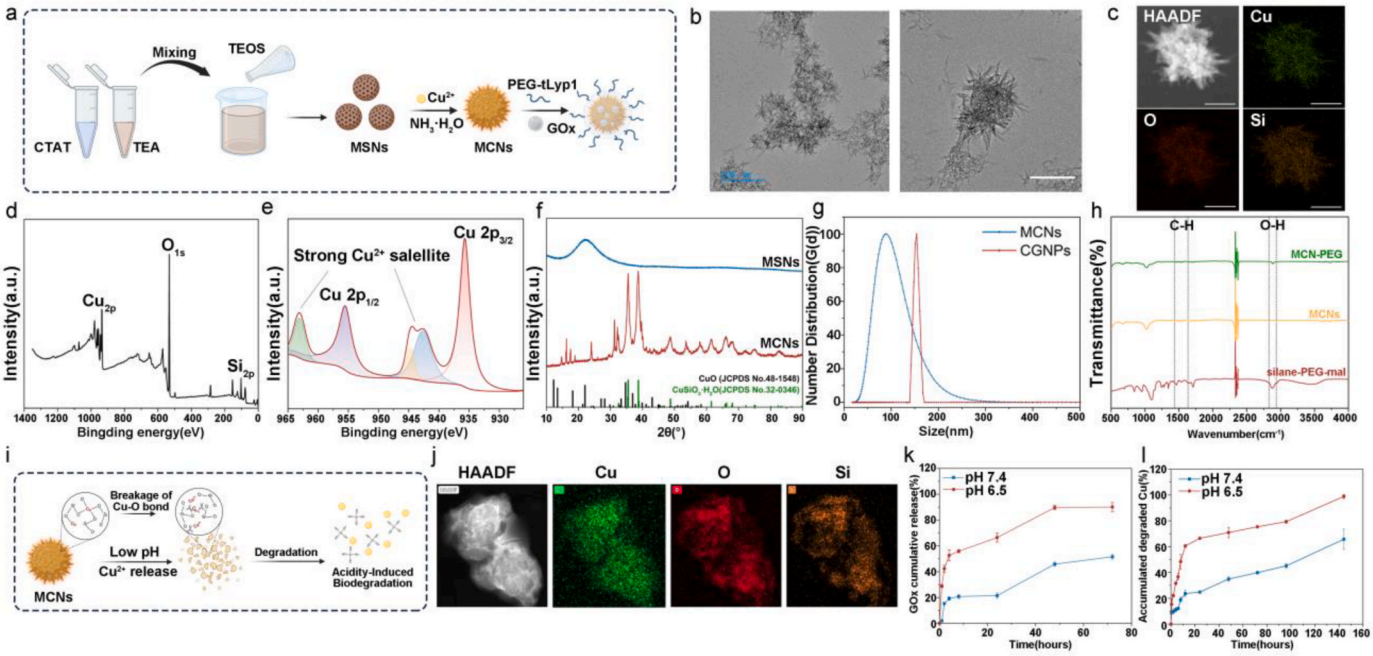

Fig. 2. Preparation and Characterization of CGNPs. a). Schematic illustration of the preparation of CGNPs; b). TEM image of MCNs (Scale bar = 200 nm); c). Elemental mapping of MCNs; d). XPS analysis of MCNs. e). High-resolution Cu 2p XPS spectra of MCNs; f). XRD patterns of MSNs(blue), MCNs(red), CuO(black) and $CuSiO_3 \cdot 3H_2O$ (green); g). Particle size of MCNs(blue) and CGNPs(red); h). FT-IR of MCNs, silane-PEG-mal and CGNPs; i). Schematic illustration of the degradation behavior of MCNs; j). Elemental mapping of degradation MCNs; GOx (k) and Cu^{2+} (l) release curves of CGNPs over time at different pH values (red: pH 6.5, blue: pH 7.4).

cuproptosis. CGNPs consume GSH through a series of cascade reactions to convert CGNPs-loaded GOx self-supplied low-toxicity $O_2^{\cdot-}$ and H_2O_2 into high-toxicity ·OH, further amplifying oxidative stress (Fig. 3a). The detection of H_2O_2 levels (Fig. 3b) showed that only a small amount of H_2O_2 was produced by CGNPs incubated with glucose in neutral whereas increased significantly in weakly acidic, and to decrease with the addition of GSH (5 mM and 10 mM), suggesting that the accumulation of H_2O_2 was inhibited considerably by excess GSH. Glutathione is tumor cells' most important endogenous antioxidant and copper chelator, significantly inhibiting ROS production and curbing cuproptosis. 5,5′-dithiobis (2-nitrobenzoic acid) (DTNB) was used as a GSH indicator to explore the ability of CGNPs to deplete GSH. As shown in Fig. 3c, the disulfide bond of DTNB was broken to form 2-nitro-5-thiobenzoic acid anion (TNB^{2-}) with GSH, and the reaction solution showed a characteristic absorption peak at 412 nm. With the addition of MCNs and CGNPs, the intensity of the TNB^{2-} absorption peak decreased (Fig. 3d). This was due to the reduction reaction of Cu^{2+} with glutathione, which the GOx further drove. Subsequently, we detected extracellular ·OH generation by a methylene blue (MB) discoloration assay (Fig. 3e) to verify the peroxidase ability of CGNPs, and in the presence of CGNPs and H_2O_2, the absorbance at 660 nm gradually decreased with the extension of the reaction time under acid condition (Fig. 3f), suggesting that CGNPs catalyzed the ·OH production, which was attributed to that GOx promotes the production of H_2O_2. At the same time, Cu^{2+} decomposes H_2O_2 into O_2, thus achieving a self-supply of oxygen, and the cycle encourages the consumption of glucose by GOx.

Effective cellular uptake is a prerequisite for tumor therapy. Therefore, we ligated tLyp-1 on PEG outside. tLyp-1 (CGNKRTR) is a homing penetrating peptide that penetrates tumor vasculature and stroma and is highly expressed on the surface of breast cancer cells. Firstly, we labeled CGNPs with FITC and analyzed cellular internalization by CLSM. With increasing incubation time, CGNPs were rapidly taken up by the MDA-MB-231 (Fig. S3) and 4T1 (Fig. S4). Flow cytometry showed that the cellular uptake of CGNPs modified by tLyp-1 reached 90.83 % after 2h, which was more substantial than not modified by tLyp-1 (74.45 %) (Fig. S3). Subsequently, we analyzed the subcellular localization of CGNPs by staining lysosomes with Lysotracker blue (Fig. S5) and further verified by Bio-TEM (Fig. 3h), which showed that CGNPs were firstly uptake by lysosomes and escape about 4 h. A necessary condition for CGNP-induced cuproptosis is the release of Cu^{2+} into the cytoplasm, which is then reduced to Cu^{+} and interacts with DLAT in the mitochondria, causing oligomerization and contributing to cell death. Therefore, we next verified that Cu+ is indeed released into the cytoplasm by staining and colocalization analysis for Cu+ and subcellular organelles (Fig. 3g and Fig. S6). The results showed that CGNPs begin to release Cu^{+} into the cytoplasm after being endocytosed for 4 h, ensuring subsequent cuproptosis. As for solid tumors, although the nano-delivery system can cross the vascular endothelium through the EPR effect, it stays in the vicinity of the blood vessels, but many regions in tumors lack microvessels, which limits the targeted delivery system. Therefore, the penetration of targeted delivery systems is extremely important for effectively treating solid tumors. In this study, we established three-dimensional spheroids of MDA-MB-231 cells to verify the tumor penetration ability of CGNPs modified by tLyp-1. The results showed that after co-incubating the CGNPs with the tumor spheres for 12 h (Fig. 3i), the tLyP-1-CGNPs could reach more than 80 μm away from the bottom of the tumor spheres. In contrast, the NPs unmodified by tLyp1 were only distributed in the superficial layer of the tumor spheres (40 μm), suggesting that the tLyP-1 peptide could facilitate the penetration of CGNPs into the deeper of the tumor.

3.4. Verification of antitumor mechanism of CGNPs-mediated cuproptosis

We next verified the cell killing effect of CGNPs on MDA-MB-231. Firstly, MDA-MB-231 cells were treated with GOx, MCNs and CGNPs, respectively. The CGNPs showed excellent cell-killing effect compared with GOx or MCNs alone (Fig. 4a). Subsequently, we performed calcein-AM/propidium iodide (CAM/PI) staining (Fig. 4b) and flow cytometry (Fig. 4c) on treated MDA-MB-231 cells, and the apoptosis rate induced by CGNPs was 92.11 %, which was much higher than that of MCNs

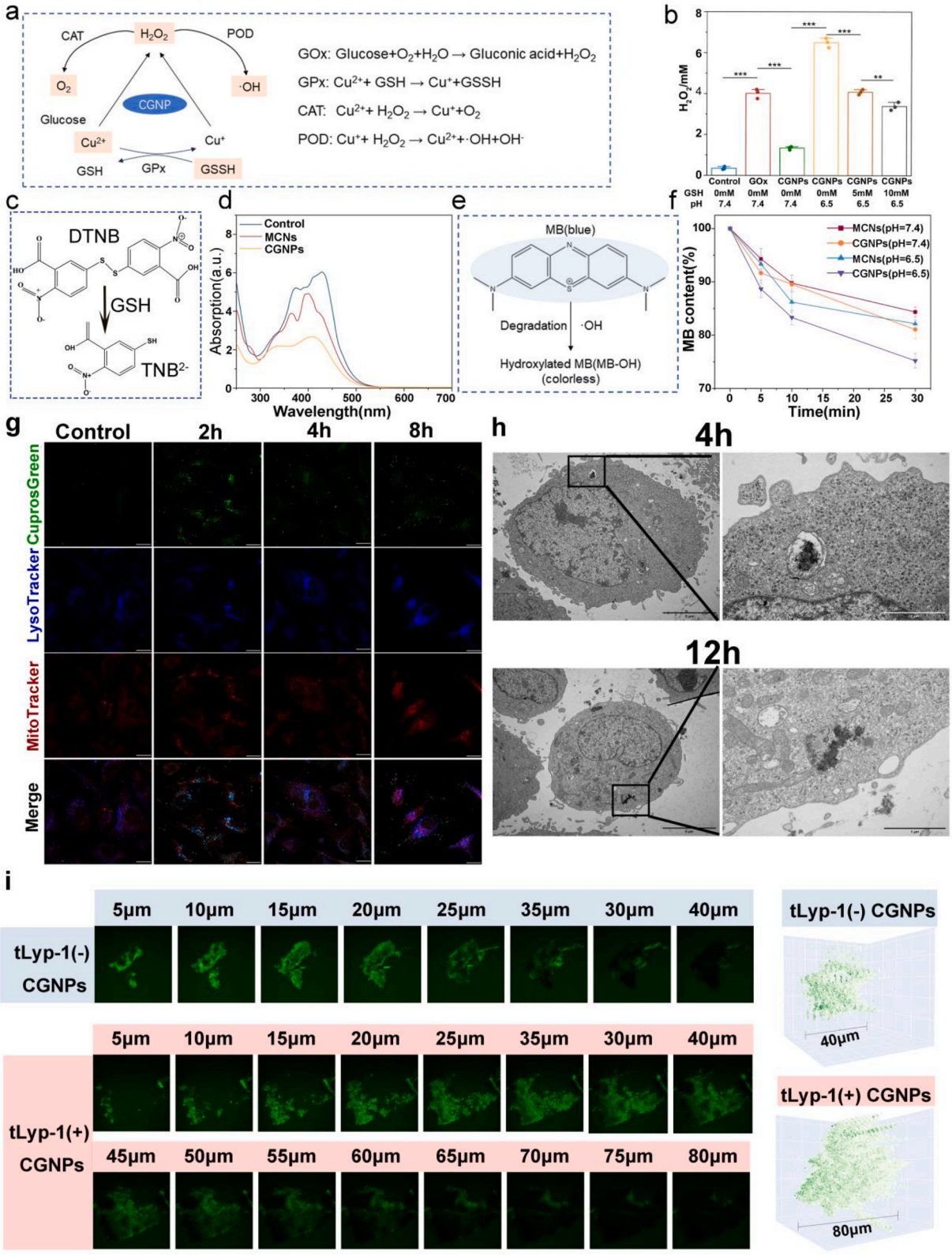

Fig. 3. Self-accelerating and cell phagocytosis of CGNPs in vitro. a). Schematic of the self-accelerating for CGNPs; b). Detection of hydrogen peroxide production by assay kits in varies conditions; c). The reaction of colorless DTNB with GSH to form the yellow product (GSH detection); d). GSH depletion by MCNs and CGNPs; e). The reaction of MB with •OH; f). Proportion of MB degradation with different treatments in pH 6.5 and 7.4; g). CLSM images of MDA-MB-231 after incubation with CGNPs for 0, 2h, 4h and 8h, respectively, stain Cu+ with CuprosGreen (green), lysosome with Lysotracker (blue) and mitochondria with Mitotracker (red) (Scale bar = 20 μm); h). Bio-TEM images of MDA-MB-231 cells after different treatments for 4h (up) and 12h (down), respectively (Left scale bar = 5 μm, Right scale bar = 1 μm); i). Three-dimensional reconstruction of the MDA-MB-231 spheroids model incubated with FITC-labeled tLyP-1-CGNPs or CGNPs.

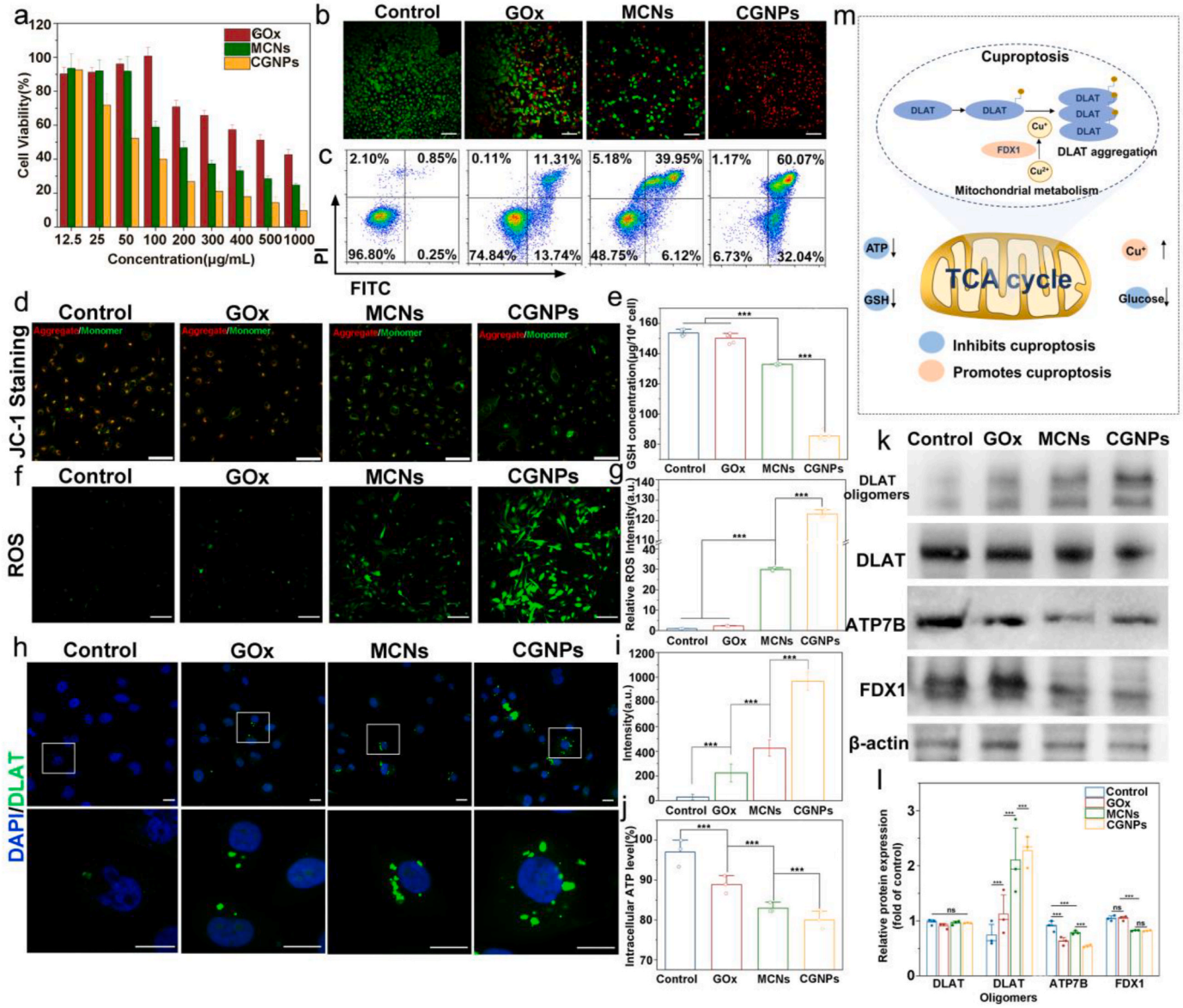

Fig. 4. In vitro cytotoxicity and cuproptosis mechanism studies of control, GOx, MCNs and CGNPs treatment groups. a). CCK-8 assay showing the cell viability of different treatment of MDA-MB-231 cells in groups; b). CLSM image of live/dead cells (Scale bar = 100 μm); c). Flow cytometry analysis of MDA-MB-231 cells apoptosis after different treatments; d). CLSM observation on the changes in the mitochondrial membrane potential of MDA-MB-231 cells after treatments. Red fluorescence: JC-1 aggregates for normal mitochondria; Green fluorescence: JC-1 monomers for damaged mitochondria with declined mitochondrial membrane potential (Scale bar = 100 μm); e). Intracellular GSH level of MDA-MB-231 cells after 24 h of different treatments; f). Intracellular ROS level of MDA-MB-231 cells in different groups by CLSM; g). Intracellular ROS level in different groups; h). Immunofluorescence images of DLAT in MDA-MB-231 cells after treatment (Scale bar = 10 μm); i). Corresponding DLAT fluorescence intensity assessment; j). The release of ATP in different groups; k). Western Blot analysis of DLAT, DLAT oligomers, FDX-1, ATP7B level after treatments and quantitative analysis results(l); m). Schematic illustration of the possible mechanism of self-accelerating of CGNPs in promoting cuproptosis. Different groups are Control, GOx, MCNs and CGNPs respectively. Data were presented as mean ± S.D. (n = 3). Statistical significance was assessed by an unpaired Student's two-sided *t*-test. *p < 0.05, **p < 0.01, ***p < 0.001.

(46.07 %) and GOx (25.05 %). To verify whether CGNPs are also toxic to normal cells, we performed a comparative analysis using the MCF-10A (normal mammary epithelial cells) and HMEC-1 (human microvascular endothelial cells) (Figs. S7 and S8). The results showed that CGNPs have only a slight toxic effect on normal cells at therapeutic doses. The above results indicated that due to the antioxidant defense and metabolic compensation of TNBC, neither cuproptosis nor starvation alone could achieve satisfactory results, while the combination of the two showed superior cell killing power.

Therefore, we subsequently examined the basis for the cytotoxicity of varies treatment (contain GOx, MCNs and CGNPs), focusing on the self-accelerating starvation therapy-cuproptosis strategy. Assessment of GSH depletion (Fig. 4e) indicated that GOx alone did not scavenge GSH, whereas MCNs induced a slight reduction due to Cu^{2+} aggregation with GSH sulfhydryl groups. CGNPs, however, disrupting GSH-Cu chelation and facilitating cuproptosis initiation. Critically, GOx on glycolysis led to a decrease in intracellular ATP (Fig. 4j). ATP, a primary intracellular energy source, also influences the expression of ATP7B, the key copper efflux protein. Therefore, given the stringent metabolic regulation in tumor cells, maintaining elevated intracellular copper levels-a prerequisite for cuproptosis-is typically challenging and the self-accelerating strategy may resolve the challenge.

Based on the above data, we provided evidence for CGNPs inducing proteotoxic stress in TNBC. Initially, we confirmed the cuproptosis-

mediated disruption of mitochondrial membranes using JC-1 fluorescent probe (Fig. 4d), revealed a weak signal corresponding to JC-1 monomers and a strong signal corresponding to JC-1 aggregates in the control group. However, the largest number of monomers and the weakest aggregation signal were observed after CGNPs treatment, indicating an obvious reduction in the mitochondrial membrane potential. Next, we showed that CGNPs enhance intracellular ROS production (Fig. 4f and g), due to a consequence of H_2O_2 generation via GOx activity, with subsequent formation of ·OH in the presence of Cu^+. Proteotoxic stress primarily arises from the direct interaction of Cu^+ with DLAT, promoting its oligomerization within the mitochondrial respiratory chain (Fig. 4h and i and Figure S9). Western blot analysis (Fig. 4k and l) further revealed significant down-regulation of FDX1 and ATP7B by CGNPs. FDX1, a pivotal protein in cuproptosis, reduction confirmed the proteotoxic stress induced by CGNPs, while the decreased expression of ATP7B sustained the cuproptosis process. CGNPs can specifically disintegrate in the TME, thereby targeting the release of Cu^{2+} and GOx loaded therein, generating H_2O_2 (facilitating ·OH production), depleting GSH (disrupting cellular antioxidant defenses), and inhibiting ATP production (down-regulating ATP7B), as shown in Fig. 4m, the prolonged and full release of copper ions, the reduction of GSH and the inhibition of glycolytic form a closed-loop cascade system that reinforces cuproptosis. The Cu^{2+} released from the CGNPs is reduced to Cu^+ by GSH and FDX1, which subsequently induces DLAT oligomerization, increases protein stress toxicity, and ultimately leads to cell death.

In summary, the mechanism by which CGNPs trigger the starvation treatment-cuproptosis self-accelerating cycle is as follows: (1) CGNPs act as acid-responsive, highly selective “tumor bombs” that are activated by the weakly acidic TME, releasing the encapsulated GOx and Cu^{2+}; (2) GOx accelerates lactate production, leading to cellular acidification and elevated H_2O_2 levels; (3) elevated acidity further ignited of CGNPs; (4) GOx drives mitochondrial respiration of TNBC, sensitizing the cells to cuproptosis; (5) Cu^{2+} reacts with H_2O_2 to generate highly toxic hydroxyl radicals (·OH) and the cuproptosis-inducing central valence state, Cu^+; (6) the presence of high valence metal ions (Cu^{2+}) leads to GSH depletion, disrupting cellular antioxidant defense; (7) starvation treatment in tumour cells is characterized by glycolysis inhibition (prompting mitochondrial respiration) and ATP supply blockade (reduced ATP7B expression), resulting in intracellular copper accumulation, which initiates cuproptosis through DLAT oligomerization and Fe-S protein cluster disruption. This process establishes a self-accelerating cycle of starvation therapy-cuproptosis with potent antitumor efficacy.

3.5. CGNPs-induced proteotoxicity promotes ICD and mtDNA release for innate immunity and adaptive immunity activation in vitro

CGNPs elicit an immune response via induction of immunogenic cell death (ICD) and the secretion of damage-associated molecular patterns (DAMPs), thereby activating antigen-presenting cells (APCs) [30,31]. We initially assessed the membranous calreticulin (CRT) and nuclear HMGB1 expression in MDA-MB-231 cells treated with GOx, MCNs and CGNPs, noting significant CRT aggregation and HMGB1 down-regulation within the CGNPs group (Fig. 5b) than other groups, which is characteristic of DAMPs. Following this, we hypothesized that proteotoxic stress compromises mitochondrial integrity, leading to mitochondrial DNA (mtDNA) release post-cuproptosis. Utilizing PicoGreen and MitoTracker Orange to stain dsDNA and mitochondria, respectively (Fig. 5f), we observed diffuse green fluorescence in the cytoplasm of CGNPs-treated cells, indicative of mtDNA release. Inspired by the fact that microbial DNA within eukaryotic cells activates the cGAS-STING signaling [32], we postulated that cytosolic mtDNA in 4T1 cells would similarly activate this pathway as a self-cGAS agonist [13]. To verify the activation of the cGAS-STING pathway after proteotoxicity-related mtDNA release, we performed western blot to analyze the expression level of STING and the phosphorylation levels of STING (labeled as p-STING). CGNPs hardly affected the expression of STING but increased the levels of p-STING (Fig. 5d and e), but not show in GOx and MCNs treatment group. Addition, ELISA kit was used to detect the levels of IFN-β (a typical type I IFN cytokine) and IL-6 [32,33] in the 4T1 cell culture medium. The results showed that CGNPs group showed the highest level of both releases (Fig. 5c). These findings substantiate that CGNPs-induced mtDNA release facilitates robust activation of the mtDNA-cGAS-STING signaling axis [32].

We examined the facilitation of dendritic cell activation and macrophage polarization. Bone marrow-derived dendritic cells (BMDCs) and bone marrow-derived macrophages (BMDMs) were derived from murine bone marrow cells and co-cultured with pretreated tumor cells in transwell inserts for 48 h. Phenotypic analysis of APCs was conducted via flow cytometry (Fig. 5g), and cytokine was detected using ELISA. The maturity of BMDCs was verified by triple staining for CD86, CD80 and CD11c (immature DCs: $CD86^-$, $CD80^-$, CD11c+; mature DCs: $CD86^+$, $CD80^+$, $CD11c^+$) (Fig. 5j and k). The results showed that CGNPs treatment significantly enhanced the proportion of mature DCs (20.89 % in the control group, 50.95 % in the GOx group, 57.39 % in the MCNs group, and 77.93 % in the CGNPs). Mature DC-associated cytokines were also produced, including IL-12p70 (essential for T-cell response) and TNF-α (Fig. 5h). Macrophage polarization was confirmed by F4/80, CD11c, CD86 and CD206 staining (CD11c for exclusion of BMDCs, F4/80 for labeling of macrophages, M1 macrophages: M1 macrophages: $F4/80^+$, $CD11c^-$, $CD86^{high}$, $CD206^{low}$; M2 macrophages. $CD11c^-$, $CD86^{high}$, $CD206^{low}$). The results show the polarization of immunosuppressive M2 phenotype macrophages ($CD\ 206^{high}CD86^{low}$) into pro-inflammatory M1 phenotype macrophages ($CD206^{low}CD86^{high}$) with the CGNPs group. This is shown by an increase in CD86 and decreased expression of CD206 (Fig. 5l and m), accompanied by an increase in the secretion of TNF-α (a pro-inflammatory cytokine for M1-type macrophages) and IFNβ (Fig. 5i).

In summary, cuproptosis releases DAMPs by inducing ICD, and it acts on mitochondria, leading to mitochondrial rupture and the release of mtDNA, which activates the cGAS-STING pathway (Fig. 5a). These findings implicate cuproptosis as a pivotal mechanism in immune cell activation, suggesting that CGNPs effectively promote DC activation and macrophage polarization, integral to innate and adaptive immune activation and tumor cell apoptosis, remodeling immunosuppressive TME.

3.6. In vivo assessments of biosafety, metabolism and antitumor efficiency of self-accelerating starvation therapy-cuproptosis

Encouraged by the in vitro results, we performed an in vivo validation. Firstly, we examined the copper ions located in the tumor. The distribution of FITC-CGNPs in mice after 4 h of tail vein injection was observed by in vivo fluorescence (Fig. 6b), which showed that most of the tLyp-1-CGNPs could be aggregated in the tumor. Subsequently, the copper content in major organs and tumor was detected 24 h after injection (Fig. 6c), and the results showed that the copper content in tumor was the highest in the CGNPs group, which was 1.66 times higher than that in the MCNs group and 3.19 times higher than that in the control group, respectively. The results suggest that CGNPs are expected to break the in vivo use of a barrier of cuproptosis and assist cuproptosis in exerting tumor cell-killing effects.

However, safety is a top concern in the treatment of metal particles. CGNPs showed high liver accumulation at early time points (24h). Due to safety concerns, we conducted further studies on biosafety and copper ion metabolism. Firstly, the hemolysis test demonstrated the good biocompatibility of MCNs and CGNPs (Fig. S10). Next, we tested the metabolism of copper ions and assessed the biosafety in normal mice. The results showed that the MCNs and CGNPs groups exhibited non-significant biotoxicity, neither body weights nor blood biochemical indexes fluctuated significantly over the 26-day observation period, and there were no obvious pathological changes in major organs (Fig. S11).

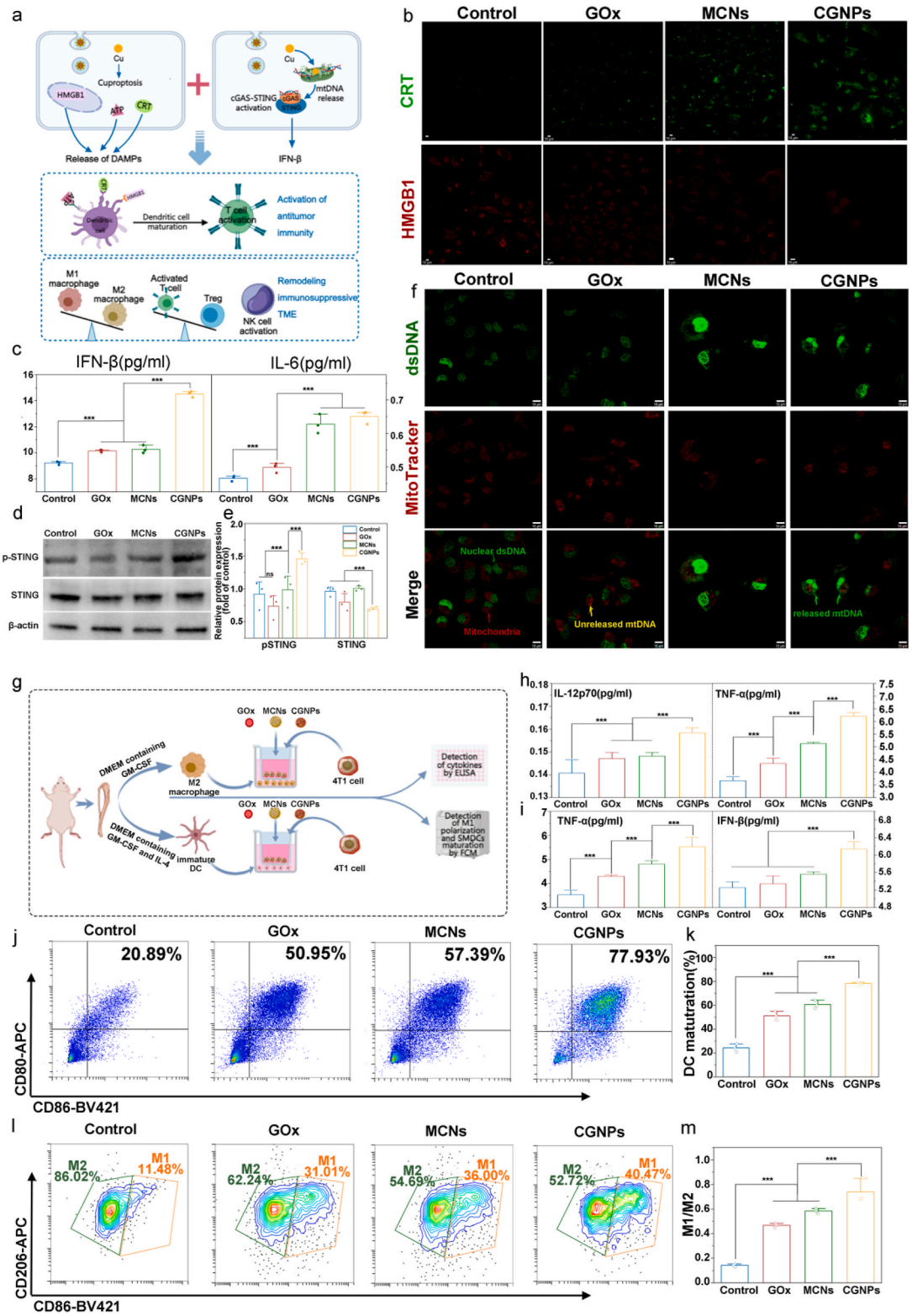

Fig. 5. In vitro immune activation mediated by GOx, MCNs, and CGNPs. a). Schematic illustration of the immunity activation of CGNPs; b). CLSM images of intracellular DAMP expression (CRT: up, HMGB1: down) after treatment; c). IFN-β (left) and IL-6 (right) release from 4T1 cells after different treatments in vitro; d). Western blot results of the expression of cGAS–STING pathway key markers after different treatments and quantitative analysis (e); f). Confocal imaging of 4T1 cells staining with PicoGreen (green) and MitoTracker Orange (red) after different treatments (Scale bar = 10 μm); g). Workflow diagram for transwell and coculture experiment; h). Mature DC-associated cytokines IL-12p70 (left) and TNF-α (right) release after different treatments; i). M1-associated cytokines TNF-α (left) and IFN-β(right) release after different treatments; j). Flow cytometry analysis of BMDCs activation, characterized by CD86 and CD80 expression gated on CD11c + cells; k). Quantitative analysis of DC maturation; l). Flow cytometry analysis of M1 ($CD86^{high}CD206^{low}$) and M2 ($CD86^{low}CD206^{high}$) BMDMs populations gated on F4/80+ cells; m). Quantitative analysis of M1/M2 radio. Different treatments are Control (blue), GOx (red), MCNs(green) and CGNPs(yellow) respectively. Data were presented as mean ± S.D. (n = 3). Statistical significance was assessed by an unpaired Student's two-sided *t*-test. *p < 0.05, **p < 0.01, ***p < 0.001.

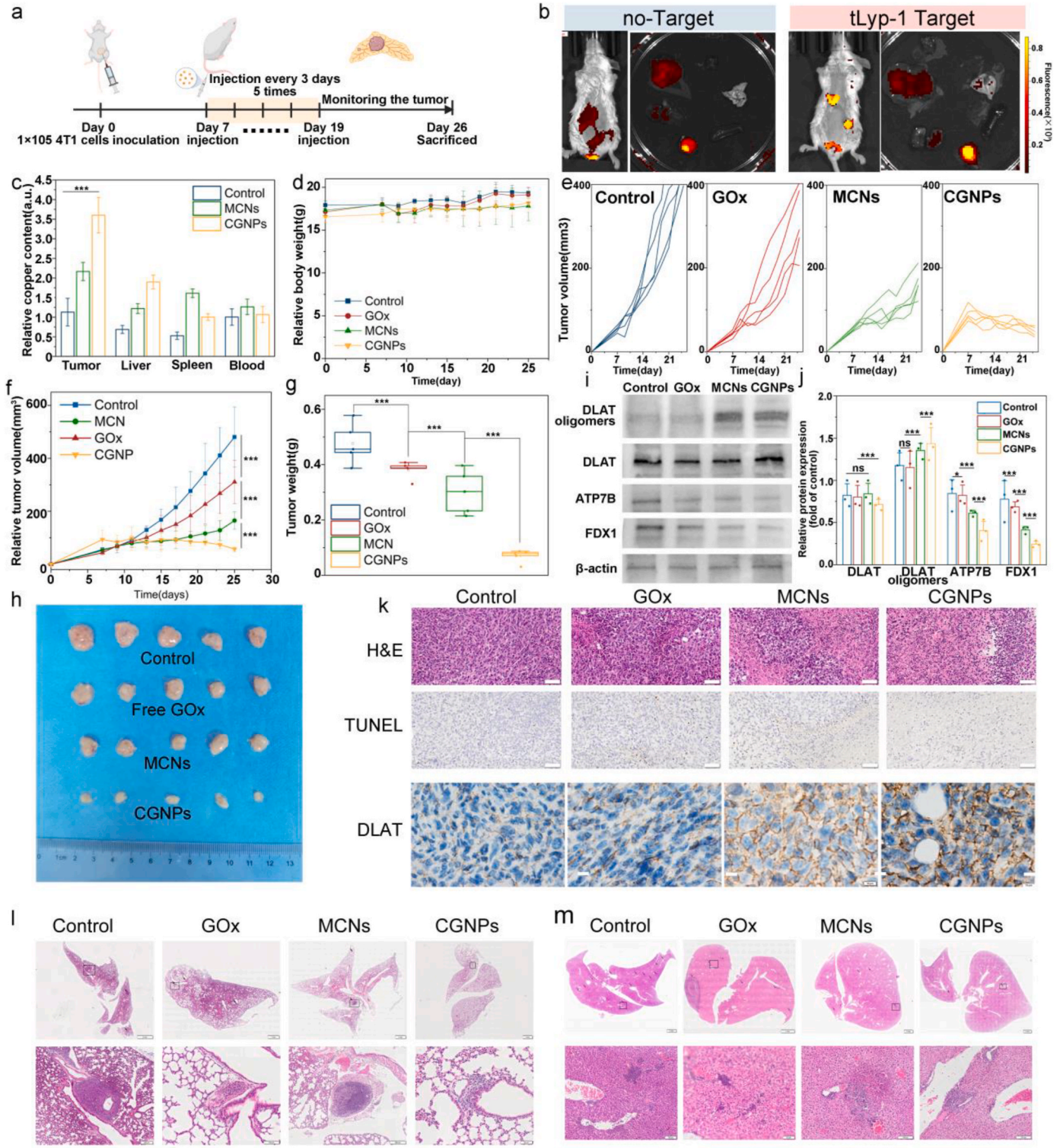

Fig. 6. Antitumor efficiency of GOx, MCNs and CGNPs in vivo. a). Schematic illustration of therapeutic experiment; b). In vivo fluorescent imaging of 4T1 tumor-bearing mice with intravenous injection of no-target-CGNPs and tLyp-1-CGNPs after 4h; c). Detection of copper in organs and tumors 24 h after injection of CGNPs by ICP-OES; d). Body weight of mice during treatment. Data were presented as mean ± S.D. (n = 5); e-f). Tumor growth curves from days 1–26. Data were presented as mean ± S.D. (n = 5); g). Weight of isolated tumors after treatment. Data were presented as mean ± S.D. (n = 5); h). Image of the isolated tumor at the end of therapy; i-j). Western blot and quantitative analysis of tumor tissue at the end of treatment. Data were presented as mean ± S.D. (n = 5); k). H&E (Scale bar = 50 μm), TUNEL (Scale bar = 50 μm), and DLAT-stained (Scale bar = 10 μm) images of tumor sections from each group of mice; H&E sections of lung(l) and liver(m) of tumor-bearing mice with different treatments. Different treatments are Control, GOx, MCNs and CGNPs respectively. Data were presented as mean ± S.D. (n = 3). Statistical significance was assessed by an unpaired Student's two-sided *t*-test. *p < 0.05, **p < 0.01, ***p < 0.001.

However, it is worth noting that the body weight of the GOx-treated group decreased slightly, suggesting that free GOx may have had some effects on the mice (Fig. S11c). Next, we injected CGNPs (10 mg/kg, 100 μL) into healthy mice and observed the metabolism of copper ions in the blood, liver, and kidney at 0, 1, 5, 7, and 15 days post-injection (Fig. S12). The data showed that although the nanomaterials unavoidably accumulated in the liver (3.43-fold the normal level) and showed slight release in the blood (1.94-fold the normal level), there was a significant decrease in copper ions in both the liver and blood after 5 days. Copper ions in the liver decreased to 1.88 times and in the blood to 1.28 times the normal level, which converged to normal levels, suggesting that copper ions were metabolized within 5 days and had no obvious toxic effects on normal tissues.

We continued to follow up on the metabolism of copper ions in 4T1 tumor-bearing mice and performed ICP-OES measurements in the tumor, liver, and blood on days 1, 3, 5, 7, and 14, respectively (Fig. S13). Copper ions remained in the tumor tissue for a longer period compared to the blood and liver and returned to normal levels after 14 days. In the liver, the copper ion levels returned to normal within 5 days, and even on the first day, it was only 1.35 times the normal level. In the blood, the copper ion levels showed only a transient increase on the first day and then returned to normal levels within 3 days. This also indicated that CGNPs maintained a relatively safe level in the mice. Nonetheless, there are differences between human and mouse metabolism, and future studies on human metabolism need to be further investigated.

Subsequently, we investigated the in vivo antitumor effect of GOx, MCNs and CGNPs using 4T1-bearing mice (Fig. 6a). Analysis of the tumor growth curves (Fig. 6e and f) revealed that the PBS and GOx groups grew rapidly. In contrast, the MCN group played a slight inhibitory role, and the CGNP group received a significant inhibition of tumor growth, which was attributed to the acceleration of the self-circulation of starvation treatment-cuproptosis. The antitumor efficacy of CGNPs was further confirmed by the tumor weight (Fig. 6g), which showed the highest tumor inhibition (85.32 %) and the lowest mean tumor weight (0.07 g).

To demonstrate the mechanism of the anti-tumor effect, we carried out a comprehensive analysis of the pathologist in the tumor tissues using H&E and immunohistochemical staining with TUNEL and DLAT (Fig. 6k). The results showed that the CGNPs group exhibited the most severe nuclear crumpling, fragmentation and deletion, accompanied by the most apparent apoptotic signals. In addition, DLAT oligomerization was most severe in tumor sections, suggesting that cuproptosis could be effectively induced. These findings provide compelling pathological evidence supporting the robust therapeutic efficacy of CGNPs by self-accelerating starvation therapy-cuproptosis strategy, which was further validated by WB (Fig. 6i and j). More notably, we performed H&E staining of the major organs in different treatment groups (Fig. S14). Due to the metastatic nature of TNBC, multiple metastatic foci were observed in both lungs (Fig. 6l, Fig. S15) and livers (Fig. 6m, Fig. S15) of the control group, especially around blood vessels, but interestingly we found that both livers and lungs in the CGNPs group compared to the other groups only few metastatic nodules were present, suggesting that the treatment of our CGNPs may be able to inhibit tumor metastasis and provide more possibilities for future treatment. Meanwhile, we recorded the survival times of each treatment group at the end of the treatment (Fig. S16). The results showed that the survival time after CGNP treatment (28.4 days) was significantly longer than that of the control (9 days), the GOx (13.8 days), and the MCNs group (23 days). This suggests that CGNPs may extend the survival of mice through tumor therapy and immune activation.

3.7. CGNPs activate the innate and adaptive immune response in vivo

Subsequently, we established a TNBC mice model to examine the capacity of CGNPs to elicit innate and adaptive immune responses. To treat mice under different conditions (containing GOx, MCNs and CGNPs), tumor tissue, lymph nodes, and spleen were collected on the 2nd day after the final treatment, tumor and lymph nodes were collected on the 14th days after the final treatment. In light of prior in vitro evidence suggesting CGNP-induced immunity activation through ICD and the cGAS-STING pathway (Fig. 7a), we investigated and validated the immune activation pathways in vivo.

Firstly, immunofluorescence analysis revealed augmented CRT exposure and aggregation in tumor cells after CGNPs treatment, concomitant with a marked reduction in nuclear HMGB1, indicative of DAMP release during ICD progression (Fig. 7b and Fig. S17). Subsequent staining for $CD4^+$ and $CD8^+$ on tumor sections confirmed an elevation of tumor-infiltrating T cells following self-accelerating CGNPs therapy (Fig. 7c). Flow cytometry quantified this increase, with $CD4^+$ T cells rising from 3.71 % (control group) to 16.27 % (CGNPs group) and $CD8^+$ T cells from 7.67 % (control group) to 22.44 % (CGNPs group), correlating with diminished tumor cell proliferation (Fig. 7d and Fig. S18). Terminal analysis of draining lymph nodes revealed a slight enhancement in the maturation rate of DCs in the GOx (12.03 %) and MCNs (14.99 %) groups compared to controls (8.98 %), with a significant rise to 21.62 % in the CGNPs group (Fig. 7f and Fig. S20). The polarization state of macrophages (M1/M2 ratio) within draining lymph nodes of the CGNPs group from an immunosuppressive M2 ($CD206^{high}CD86^{low}$) to a pro-inflammatory M1 phenotype ($CD206^{low}CD86^{high}$), from 0.47 of control group, 0.54 of GOx group, 1.31 of MCNs groups and 2.25 of CGNPs group (Fig. S19).

Secondly, CGNPs are anticipated to potentiate adaptive immune responses via the cGAS-STING pathway. Flow cytometric analysis of tumor-infiltrating NK cells ($CD45+CD3^-CD49b+$) revealed an increase from 6.59 % in the control group to 20.77 % in the CGNPs group (Fig. S21), indicating the efficacy of the starvation treatment-cuproptosis self-accelerating cycle in stimulating innate anti-tumor immunity. In addition, the CGNPs group displayed in tumors TNFα (a key indicator of anti-tumor cellular immunity and direct tumor cell killing [34]), IL-12p70 (required for T-cell response [11]), IFN-γ (an important cytokine associated with anti-tumor immunity by $CD8^+$ T cell [35]), IL-6 (a key marker of humoral immunity related to T-cell differentiation and synergistic co-signal provider [36]) and IFN-β(activates NK cells and improves their cytotoxic activity [37])secretion levels all showed a more pronounced increase (Fig. S22), with IFN-β and IL-12p70 being essential for stimulating NK cells, and IL-6, TNFα and IFN-γ being essential for activating tumor adaptive immunity, corroborating the role of CGNPs in activating both innate and adaptive immune responses via the cGAS-STING pathway.

Additionally, we evaluated the potential of CGNPs to induce a long-term immune memory effect. First, we quantification of splenic effector memory T cells (Tem, $CD3^+CD8^+CD44+CD62L-$) and central memory T cells (Tcm, $CD3^+CD8^+CD44+CD62L+$) by FCM (Fig. 7g), the relative proportions of Tem and Tcm exhibited the obvious increase in the CGNPs group, especially Tem. Among them, Tem cells can retain the memory of the antigen for a long time, whereas Tcm cells indicate that the organism can rapidly initiate an immune response upon re-infection. Therefore, to further validate the long-term immune response ability induced by CGNPs, we measured the infiltration of $CD4^+$ and $CD8^+$ T cells in the tumor tissues and the maturation of DC cells in the lymph nodes 14 days after the treatment had ended. The results showed that although there was a decrease in the infiltration of T cells in the tumor 14 days later, the CGNPs group still maintained a high level compared to the other groups in terms of both $CD4^+$ (18.49 %) and $CD8^+$ (17.62 %) cell infiltration (Fig. 7h and i). Similarly, the highest rate of DC cell maturation (12.95 %) was observed in the lymph nodes (Fig. S23). Thus, corresponding to the splenic memory cell assay, suggesting that CGNPs-mediated multiple immune activations in tumors may be able to induce long-lasting immune memory, which is conducive to the inhibition of tumor recurrence and metastasis.

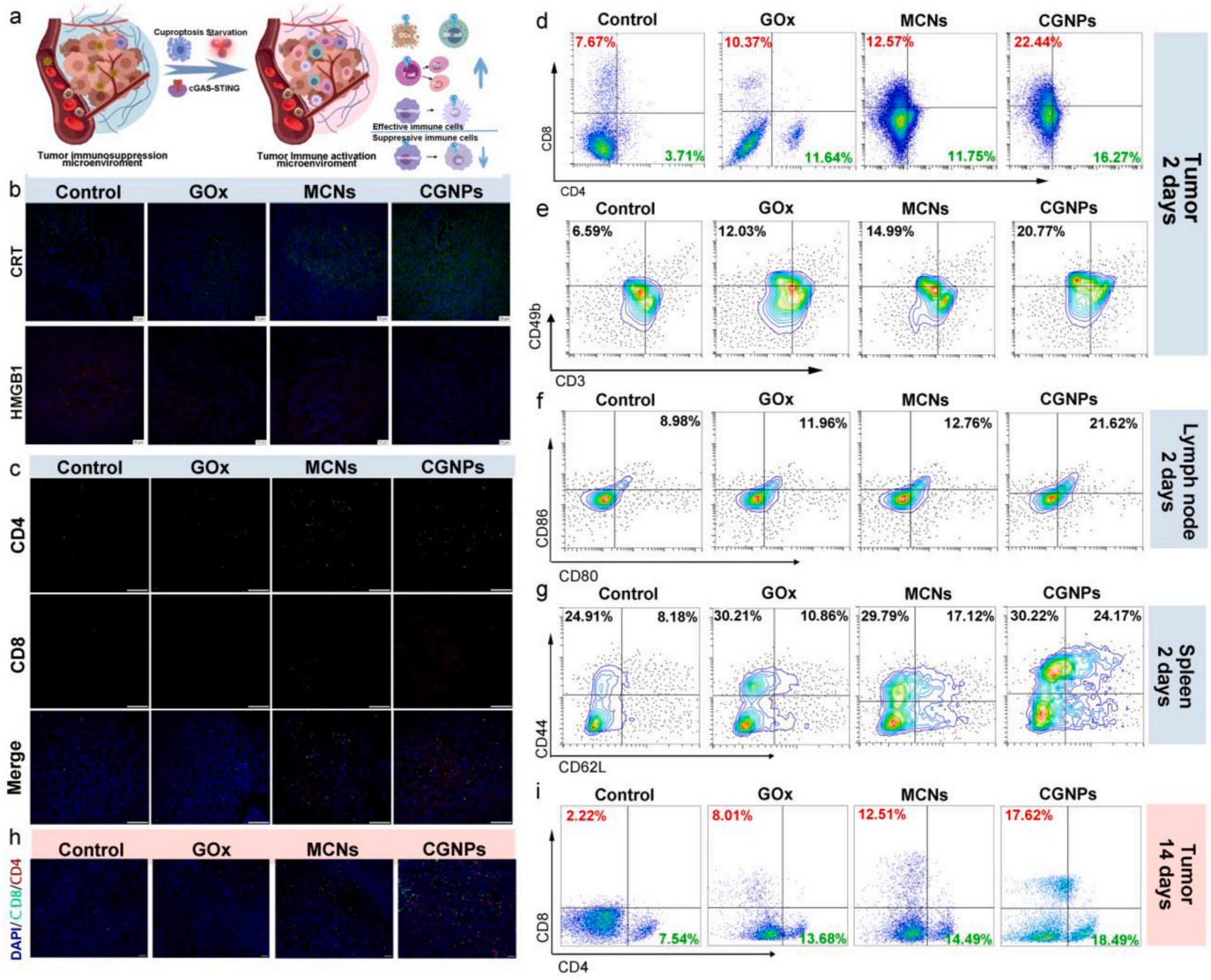

Fig. 7. Innate and adaptive immune responses induced by GOx, MCNs, and CGNPs in vivo. a). Schematic illustration of the immunity response in vivo; b). Immunofluorescence staining of CRT and HMGB1 in tumor tissue sections at the end of treatment (Scale bar = 10 μm); c). Immunofluorescence staining of $CD4^+$ T cells (green) and $CD8^+$ T cells (red) in tumor tissue sections at 2 days after the end of treatment using CLSM (Scale bar = 100 μm); d). $CD8^+$ T cells and $CD4^+$ T cells in tumor tissue by FCM; e). CD49b + $CD3^-$ $CD45^+$ cells in tumor tissue by FCM; f). CD80+$CD86^+$ cells (Matura DC) in lymph node; g). Representative flow cytometry plots of the effector memory T cells (Tem) and the central memory T cells (Tcm) in the spleens of mice after treatments; h). Immunofluorescence staining of $CD4^+$ T cells (green) and $CD8^+$ T cells (red) in tumor tissue sections at 14 days after the end of treatment using CLSM (Scale bar = 100 μm); i). $CD8^+$ T cells and $CD4^+$ T cells in tumor tissue at 14 days after the end of treatment by FCM. Different treatments are Control, GOx, MCNs and CGNPs, respectively. Data were presented as mean ± S.D. (n = 3). Statistical significance was assessed by an unpaired Student's two-sided *t*-test. *p < 0.05, **p < 0.01, ***p < 0.001.

4. Conclusions

In summary, Cu^{2+} was successfully incorporated into the MSNs framework using a straightforward hydrothermal approach. It thus can be degraded under weakly acidic conditions, and its sea urchin-like structure allows for loading GOx for self-accelerating starvation therapy-cuproptosis for antitumor therapy and activating immunity. The cuproptosis self-amplification effect and immune activation ability of CGNPs were verified by in vivo and vitro studies, and the specific mechanisms are summarized as follows: (1) CGNPs act as acid-responsive, highly selective "tumor bombs" that are triggered by the specific weakly acidic TME to release the encapsulated GOx and Cu^{2+}; (2) GOx induces cellular acidification and elevated H_2O_2 levels; (3) The elevated acidity further activates the degradation of CGNPs, releasing Cu^{2+}; (4) GOx drives mitochondrial respiration of TNBCs, which sensitizes the onset of cuproptosis; (5) the reaction of Cu^{2+} with H_2O_2 produces the highly toxic ·OH and the cuproptosis-inducing central valence state, Cu^+; (6) The presence of high valence metal ions (Cu^{2+}) leads to GSH depletion and disruption of cellular antioxidant defense mechanisms; (7) Starvation therapy is characterized by inhibition of glycolysis (promoting mitochondrial respiration) and blocked ATP supply (decreased ATP7B expression), resulting in intracellular copper accumulation, which initiates cuproptosis through DLAT oligomerization and Fe-S cluster disruption; (8) Oxidative damage-mediated apoptosis leads to ICD, promoting immune activation (DC cell maturation) through the release of DAMPs; (9) Enhancing cuproptosis release mtDNA and activation cGAS-STING pathway, converting immunosuppressed TME into immune-activated ones. In conclusion, our analysis of clinical samples and public databases reveals that the immune microenvironment of TNBC is biased towards 'cold' tumors, which limits the efficacy of immunotherapy for TNBC. Furthermore, TNBC appears to be more sensitive to cuproptosis, suggesting that cuproptosis may be a

promising strategy for the clinical treatment of TNBC. In this study, by constructing self-accelerating CGNPs, we demonstrated that cuproptosis can induce innate and adaptive immunity through immunogenic cell death and mtDNA release, thereby transforming TNBC into 'hot' tumors. This approach significantly inhibits the progression of the primary tumor and induces long-term immune memory, potentially emerging as a promising therapeutic tool for TNBC.

CRediT authorship contribution statement

Xinzhi Xu: Writing – original draft, Methodology, Funding acquisition, Data curation. **Hang Zhou:** Writing – review & editing, Visualization, Software, Data curation. **Ruixia Hong:** Writing – review & editing, Validation, Methodology. **Jiaqi Gong:** Visualization, Software, Investigation. **Yujie Wan:** Methodology, Data curation. **Qihuan Fu:** Visualization, Software. **Kaifeng Huang:** Methodology, Investigation. **Ying Li:** Data curation. **Na Wang:** Writing – original draft, Validation, Methodology. **Peng Zhao:** Writing – review & editing, Methodology, Funding acquisition. **Kaiyong Cai:** Writing – review & editing, Validation, Project administration, Conceptualization. **Fang Li:** Validation, Project administration, Funding acquisition, Conceptualization.

Ethics approval and consent to participate

All animal protocols were approved by the Ethics Review Statement of the Affiliated Chongqing University Cancer Hospital, Chongqing, China. (Ethical Permit Number: CZLS2023265-A).

Data availability

Data will be made available on request.

Declaration of competing interest

The authors declare the following financial interests/personal relationships which may be considered as potential competing interests: Xinzhi Xu reports financial support was provided by China Postdoctoral Science Foundation. Xinzhi Xu, Fang Li, Yujie Wan reports financial support was provided by Natural Science Foundation of Chongqing, China. Fang Li reports financial support was provided by Fundamental Research Funds for The Central Universities. Fang Li reports financial support was provided by Chongqing Science and Health Joint Medical Research Key Project. Peng Zhao reports financial support was provided by National Natural Science Foundation of China. If there are other authors, they declare that they have no known competing financial interests or personal relationships that could have appeared to influence the work reported in this paper.

Acknowledgment

This work was supported by the China Postdoctoral Science Foundation, China (No. 2023M740439), the Natural Science Foundation of Chongqing, China (CSTB2024NSCQ-MSX0647, CSTB2024NSCQ-MSX0460 and CSTB2022NSCQ-MSXC324), the Fundamental Research Funds for The Central Universities, China (No. 2023CDJYGRH-ZD02), the Chongqing Science And Health Joint Medical Research Key Project, China (No. 2025ZDXM015) and the National Natural Science Foundation of China (No. 82102225).

Appendix A. Supplementary data

Supplementary data to this article can be found online at https://doi.org/10.1016/j.bioactmat.2025.02.019.

References

[1] R.L. Siegel, A.N. Giaquinto, A. Jemal, Cancer statistics, CA Cancer J. Clin. 74 (1) (2024) 12–49.
[2] G. Bianchini, C. De Angelis, L. Licata, L. Gianni, Treatment landscape of triple-negative breast cancer - expanded options, evolving needs, Nat. Rev. Clin. Oncol. 19 (2) (2022) 91–113.
[3] Y. Gong, P. Ji, Y.-S. Yang, S. Xie, T.-J. Yu, Y. Xiao, M.-L. Jin, D. Ma, L.-W. Guo, Y.-C. Pei, W.-J. Chai, D.-Q. Li, F. Bai, F. Bertucci, X. Hu, Y.-Z. Jiang, Z.-M. Shao, Metabolic-pathway-based subtyping of triple-negative breast cancer reveals potential therapeutic targets, Cell Metab. 33 (1) (2021) 51–64.e9.
[4] M. Liao, R. Qin, W. Huang, H.-P. Zhu, F. Peng, B. Han, B. Liu, Targeting regulated cell death (RCD) with small-molecule compounds in triple-negative breast cancer: a revisited perspective from molecular mechanisms to targeted therapies, J. Hematol. Oncol. 15 (1) (2022).
[5] K. Fang, Z. Xu, S. Jiang, C. Yan, D. Tang, Y. Huang, Integrated profiling uncovers prognostic, immunological, and pharmacogenomic features of ferroptosis in triple-negative breast cancer, Front. Immunol. 13 (2022) 985861.
[6] A.G. Waks, E.P. Winer, Breast cancer treatment: a review, J. Am. Med. Assoc. 321 (3) (2019) 288–300.
[7] T.E. Keenan, S.M. Tolaney, Role of immunotherapy in triple-negative breast cancer, J. Natl. Compr. Cancer Netw. 18 (4) (2020) 479–489.
[8] D. Tang, X. Chen, G. Kroemer, Cuproptosis: a copper-triggered modality of mitochondrial cell death, Cell Res. 32 (5) (2022) 417–418.
[9] S.R. Li, L.L. Bu, L. Cai, Cuproptosis: lipoylated TCA cycle proteins-mediated novel cell death pathway, Signal Transduct. Targeted Ther. 7 (1) (2022) 158.
[10] L. Huang, J. Zhu, G. Wu, W. Xiong, J. Feng, C. Yan, J. Yang, Z. Li, Q. Fan, B. Ren, Y. Li, C. Chen, X. Yu, Z. Shen, A strategy of "adding fuel to the flames" enables a self-accelerating cycle of ferroptosis-cuproptosis for potent antitumor therapy, Biomaterials 311 (2024).
[11] S. Luo, Y. Yang, L. Chen, P.R. Kannan, W. Yang, Y. Zhang, R. Zhao, X. Liu, Y. Li, X. Kong, Outer membrane vesicle-wrapped manganese nanoreactor for augmenting cancer metalloimmunotherapy through hypoxia attenuation and immune stimulation, Acta Biomater. 181 (2024) 402–414.
[12] P. Tsvetkov, S. Coy, B. Petrova, M. Dreishpoon, A. Verma, M. Abdusamad, J. Rossen, L. Joesch-Cohen, R. Humeidi, R.D. Spangler, J.K. Eaton, E. Frenkel, M. Kocak, S.M. Corsello, S. Lutsenko, N. Kanarek, S. Santagata, T.R. Golub, Copper induces cell death by targeting lipoylated TCA cycle proteins, Science 375 (6586) (2022) 1254–1261.
[13] X. Yu, B. Li, J. Yan, W. Li, H. Tian, G. Wang, S. Zhou, Y. Dai, Cuproptotic nanoinducer-driven proteotoxic stress potentiates cancer immunotherapy by activating the mtDNA–cGAS–STING signaling, Biomaterials 307 (2024).
[14] Y. Li, Z. Zhu, S. Hua, Y. Wan, Q. Chen, G. Gao, H. Zhang, W. Duan, W. Zheng, Y. Guo, Q. Hu, J.-W. Shen, M. Zhou, Q. Wei, Metal-based nanoparticles promote the activation of cGAS-STING pathway for enhanced cancer immunotherapy, Nano Today 58 (2024).
[15] C. Hong, M. Schubert, A.E. Tijhuis, M. Requesens, M. Roorda, A. van den Brink, L. A. Ruiz, P.L. Bakker, T. van der Sluis, W. Pieters, M. Chen, R. Wardenaar, B. van der Vegt, D.C.J. Spierings, M. de Bruyn, M. van Vugt, F. Foijer, cGAS-STING drives the IL-6-dependent survival of chromosomally instable cancers, Nature 607 (7918) (2022) 366–373.
[16] J.L. Liang, X.K. Jin, S.M. Zhang, Q.X. Huang, P. Ji, X.C. Deng, S.X. Cheng, W. H. Chen, X.Z. Zhang, Specific activation of cGAS-STING pathway by nanotherapeutics-mediated ferroptosis evoked endogenous signaling for boosting systemic tumor immunotherapy, Sci. Bull. 68 (6) (2023) 622–636.
[17] E.L. Dane, A. Belessiotis-Richards, C. Backlund, J. Wang, K. Hidaka, L.E. Milling, S. Bhagchandani, M.B. Melo, S. Wu, N. Li, N. Donahue, K. Ni, L. Ma, M. Okaniwa, M.M. Stevens, A. Alexander-Katz, D.J. Irvine, STING agonist delivery by tumour-penetrating PEG-lipid nanodiscs primes robust anticancer immunity, Nat. Mater. 21 (6) (2022) 710–720.
[18] M. Cui, D. Tang, B. Wang, H. Zhang, G. Liang, H. Xiao, Bioorthogonal guided activation of Cgas-STING by Aie photosensitizer nanoparticles for targeted tumor therapy and imaging, Adv. Mater. 35 (52) (2023) e2305668.
[19] K. Wang, Y. Li, X. Wang, Z. Zhang, L. Cao, X. Fan, B. Wan, F. Liu, X. Zhang, Z. He, Y. Zhou, D. Wang, J. Sun, X. Chen, Gas therapy potentiates aggregation-induced emission luminogen-based photoimmunotherapy of poorly immunogenic tumors through cGAS-STING pathway activation, Nat. Commun. 14 (1) (2023) 2950.
[20] N. Wang, Y. Liu, D. Peng, Q. Zhang, Z. Zhang, L. Xu, L. Yin, X. Zhao, Z. Lu, J. Peng, Copper-based composites nanoparticles improve triple-negative breast cancer treatment with induction of apoptosis-cuproptosis and immune activation, Adv. Healthcare Mater. 13 (28) (2024) e2401646.
[21] W.Q. Liu, W.R. Lin, L. Yan, W.H. Xu, J. Yang, Copper homeostasis and cuproptosis in cancer immunity and therapy, Immunol. Rev. 00 (2023) 1–17.
[22] L. Chen, J. Min, F. Wang, Copper homeostasis and cuproptosis in health and disease, Signal Transduct. Targeted Ther. 7 (1) (2022) 378.
[23] C. Cao, N. Yang, Y. Su, Z. Zhang, C. Wang, X. Song, P. Chen, W. Wang, X. Dong, Starvation, ferroptosis, and prodrug therapy synergistically enabled by a cytochrome c oxidase like nanozyme, Adv. Mater. 34 (29) (2022) e2203236.
[24] M. Wang, M. Chang, C. Li, Q. Chen, Z. Hou, B. Xing, J. Lin, Tumor-microenvironment-activated reactive oxygen species amplifier for enzymatic cascade cancer starvation/chemodynamic/immunotherapy, Adv. Mater. 34 (4) (2022) e2106010.
[25] B. Guo, F. Yang, L. Zhang, Q. Zhao, W. Wang, L. Yin, D. Chen, M. Wang, S. Han, H. Xiao, N. Xing, Cuproptosis induced by ROS responsive nanoparticles with elesclomol and copper combined with αPD-L1 for enhanced cancer immunotherapy, Adv. Mater. 35 (22) (2023).

[26] Y. Huang, X. Wan, Q. Su, C. Zhao, J. Cao, Y. Yue, S. Li, X. Chen, J. Yin, Y. Deng, X. Zhang, T. Wu, Z. Zhou, D. Wang, Ultrasound-activated piezo-hot carriers trigger tandem catalysis coordinating cuproptosis-like bacterial death against implant infections, Nat. Commun. 15 (1) (2024).
[27] Z. Zhao, S. Dong, Y. Liu, J. Wang, L. Ba, C. Zhang, X. Cao, C. Wu, P. Yang, Tumor microenvironment-activable manganese-boosted catalytic immunotherapy combined with PD-1 checkpoint blockade, ACS Nano 16 (12) (2022) 20400–20418.
[28] W. Tang, J. Wu, L. Wang, K. Wei, Z. Pei, F. Gong, L. Chen, Z. Han, Y. Yang, Y. Dai, X. Cui, L. Cheng, Bioactive layered double hydroxides for synergistic sonodynamic/cuproptosis anticancer therapy with elicitation of the immune response, ACS Nano 18 (15) (2024) 10495–10508.
[29] X.-K. Jin, J.-L. Liang, S.-M. Zhang, Q.-X. Huang, S.-K. Zhang, C.-J. Liu, X.-Z. Zhang, Orchestrated copper-based nanoreactor for remodeling tumor microenvironment to amplify cuproptosis-mediated anti-tumor immunity in colorectal cancer, Mater. Today 68 (108) (2023).
[30] L. Qiu, J. Liang, L. Xue, X. Qiao, H. Xu, H. Xiang, Y. Chen, H. Ding, On-demand peroxynitrite overproduction reprograms systemic immune function for augmented sono-immunotherapy against tumor, Adv. Funct. Mater. 34 (48) (2024).
[31] X. Yu, X. Li, Q. Chen, S. Wang, R. Xu, Y. He, X. Qin, J. Zhang, W. Yang, L. Shi, L. Lu, Y. Zheng, Z. Pang, S. Peng, High intensity focused ultrasound-driven nanomotor for effective ferroptosis-immunotherapy of TNBC, Adv. Sci. 11 (15) (2024) e2305546.
[32] M. Jiang, P. Chen, L. Wang, W. Li, B. Chen, Y. Liu, H. Wang, S. Zhao, L. Ye, Y. He, C. Zhou, cGAS-STING, an important pathway in cancer immunotherapy, J. Hematol. Oncol. 13 (1) (2020) 81.
[33] M.F. Gulen, N. Samson, A. Keller, M. Schwabenland, C. Liu, S. Glück, V.V. Thacker, L. Favre, B. Mangeat, L.J. Kroese, P. Krimpenfort, M. Prinz, A. Ablasser, cGAS-STING drives ageing-related inflammation and neurodegeneration, Nature 620 (7973) (2023) 374–380.
[34] M. Cui, D. Tang, B. Wang, H. Zhang, G. Liang, H. Xiao, Bioorthogonal guided activation of Cgas-STING by Aie photosensitizer nanoparticles for targeted tumor therapy and imaging, Adv. Mater. 35 (52) (2023) e2305668.
[35] Y. Li, W. Chen, Y. Kang, X. Zhen, Z. Zhou, C. Liu, S. Chen, X. Huang, H.-J. Liu, S. Koo, N. Kong, X. Ji, T. Xie, W. Tao, Nanosensitizer-mediated augmentation of sonodynamic therapy efficacy and antitumor immunity, Nat. Commun. 14 (1) (2023).
[36] Z. Dai, X. Li, Q. Chen, Y. Zhu, Z. Shi, X. Deng, C. Wang, H. Chen, Injectable responsive hydrogel delivery platform: enabling high tissue penetration and sonogenetic-like potentiating anti-tumor immunotherapy, Adv. Funct. Mater. 34 (19) (2024).
[37] L. Zhang, S.-C. Wan, J. Zhang, M.-J. Zhang, Q.-C. Yang, B. Zhang, W.-Y. Wang, J. Sun, R.T.K. Kwok, J.W.Y. Lam, H. Deng, Z.-J. Sun, B.Z. Tang, Activation of pyroptosis using AIEgen-based sp2 carbon-linked covalent organic frameworks, J. Am. Chem. Soc. 145 (32) (2023) 17689–17699.